

Optical properties and carrier localization in the layered phosphide EuCd_2P_2 C. C. Homes^{1,*}, Z.-C. Wang,² K. Fruhling², and F. Tafti^{2,†}¹*National Synchrotron Light Source II, Brookhaven National Laboratory, Upton, New York 11973, USA*²*Department of Physics, Boston College, Chestnut Hill, Massachusetts 02467, USA*

(Received 21 September 2022; revised 10 December 2022; accepted 12 December 2022; published 5 January 2023)

The temperature dependence of the complex optical properties of the layered phosphide material EuCd_2P_2 have been measured over a wide frequency range above and below $T_N \simeq 11.5$ K for light polarized in the a - b planes. At room temperature, the optical conductivity is well described by a weak free-carrier component with a Drude plasma frequency of $\simeq 1100$ cm^{-1} and a scattering rate of $1/\tau_D \simeq 700$ cm^{-1} , with the onset of interband absorptions above $\simeq 2000$ cm^{-1} . Two infrared-active E_u modes are observed at $\simeq 89$ and 239 cm^{-1} . As the temperature is reduced the scattering rate decreases and the low-frequency conductivity increases slightly; however, below $\simeq 50$ K the conductivity decreases until at the resistivity maximum at $\simeq 18$ K (just below $2T_N$) the spectral weight associated with free carriers is transferred to a localized excitation at $\simeq 500$ cm^{-1} . Below T_N , metallic behavior is recovered. Interestingly, the E_u modes are largely unaffected by these changes, with only the position of the high-frequency mode showing any signs of anomalous behavior. While several scenarios are considered, the prevailing view is that the resistivity maximum and subsequent carrier localization is due to the formation of ferromagnetic domains below $\simeq 2T_N$ that result in spin-polarized clusters due to spin-carrier coupling.

DOI: [10.1103/PhysRevB.107.045106](https://doi.org/10.1103/PhysRevB.107.045106)**I. INTRODUCTION**

Magnetic semimetals display a variety of interesting phenomena. The layered europium materials EuCd_2X_2 , with $X = \text{Sb}, \text{As},$ and P , are of particular interest as the Sb and As materials are magnetic Weyl semimetals [1–9]. These hexagonal materials have a layered crystal structure, with the Cd_2X_2 layers separated by the europium layers; the magnetism originates from the europium layers which order antiferromagnetically at low temperature [10,11]. The transport properties of these materials are intriguing as they display peaks in the resistivity close to the Néel temperature. In the case of As ($T_N \simeq 9.5$ K), the in-plane resistivity roughly triples, while in the case of Sb ($T_N \simeq 7.4$ K), it is more of a shoulderlike feature; however, in both cases the increase occurs at T_N and is suppressed by the application of a modest magnetic field [12]. This behavior is dramatically exaggerated in the phosphide material ($T_N \simeq 11.5$ K). At room temperature, the in-plane resistivity may be described as that of a poor metal with $\rho_{ab} \simeq 25$ $\text{m}\Omega\text{cm}$; this value increases by roughly two orders of magnitude well above T_N at $\simeq 18$ K, effectively rendering the sample semiconducting; below this temperature the resistivity drops dramatically, falling slightly below the room temperature value at and below T_N [13]. As with Sb and As, the resistivity peak is suppressed with magnetic field, resulting in a colossal magnetoresistance. Key questions for the phosphide material are: What is the nature of the free-carrier response, and what becomes of the free-carriers at the resis-

tivity maximum? The optical conductivity is ideally suited to address these issues. The change in the dc conductivity from $\sigma_{dc} \simeq 65$ $\Omega^{-1}\text{cm}^{-1}$ at $\simeq 50$ K to a value that is effectively zero from an optical point of view should have a dramatic signature in the optical properties. The frequency dependence of the optical conductivity will also allow the spectral weight and the scattering rate associated with the free carriers to be determined, as well as the shifts in the spectral weight near the resistivity maximum to be tracked.

In this work the temperature dependence of the in-plane complex optical properties have been determined for a single crystal of EuCd_2P_2 over a wide frequency range for light polarized in the a - b planes. At room temperature, two infrared-active vibrational modes and a weak Drude-like free-carrier component are superimposed on an otherwise semiconducting response with an onset of absorption due to interband transitions at $\gtrsim 2000$ cm^{-1} . While the spectral weight associated with the free carriers remains roughly constant with decreasing temperature, the scattering rate decreases by about 10% between 295 and 50 K, consistent with the transport values for the resistivity. Below 50 K, the resistivity (and the scattering rate) increases by roughly a factor of two at 25 K, heralding the complete disappearance of the free-carrier component, the totality of which is transferred into a localized excitation centered at $\simeq 500$ cm^{-1} ($\simeq 62$ meV); below T_N the metallic behavior is restored and the spectral weight associated with the localized excitation is transferred back into the free-carrier response. The dramatic changes in the resistivity and the optical properties are intimately connected to the magnetism in this material. While several different possibilities are considered, it appears that formation of ferromagnetic clusters at $\simeq 2T_N$ result in carrier

*homes@bnl.gov

†fazel.tafti@bc.edu

localization in spin-polarized clusters [14]; this effect is suppressed when the clusters become contiguous and form a network. Moreover, below T_N the conductivity increases slightly, likely due to a decrease in fluctuations.

II. EXPERIMENT AND RESULTS

Single crystals of EuCd_2P_2 were grown using a flux technique that has been previously described [13]; x-ray diffraction on the large, mirrorlike crystal faces revealed that they contain the a - b planes. It should be noted that there is some terracing on the surface of the crystal. The reflectivity of an as-grown crystal face ($\simeq 1.5 \text{ mm} \times 2 \text{ mm}$) has been measured at a near-normal angle of incidence for light polarized parallel to the a - b planes over a wide temperature and frequency range ($\simeq 2 \text{ meV}$ to 4 eV) using an *in situ* evaporation technique [16]; the results are shown in Fig. 1.

The character of the reflectivity may be described as either poorly metallic, or semiconducting (insulating), depending on the temperature. The response of the reflectivity is shown in the metallic case in Fig. 1(a) at temperatures between 25 and 295 K, and at 5 K; for these temperatures the low-frequency reflectivity is increasing rapidly with decreasing frequency, which is in agreement with the requirement that when $\sigma_{dc} \neq 0$, $R(\omega \rightarrow 0) = 1$. The two prominent features in the reflectivity that are attributed to the normally infrared-active lattice modes are also partially screened [17]. In contrast, the reflectivity in Fig. 1(b) between 10 and 18 K shows a dramatically different response; $R(\omega \rightarrow 0) \simeq \text{const}$, the result expected for an insulator or semiconductor. In addition, the two lattice modes appear to be almost totally unscreened, resulting in fundamentally different line shapes [18].

The reflectivity is a combination of the real and imaginary parts of the dielectric function, and as such can be difficult to interpret; the real part of the optical conductivity, calculated from the imaginary part of the dielectric function, is a more intuitive quantity. Accordingly, the complex dielectric function, $\tilde{\epsilon}(\omega) = \epsilon_1 + i\epsilon_2$, has been determined from a Kramers-Kronig analysis of the reflectivity [19], which requires extrapolations at high and low frequency. In the case where metallic conductivity is observed, at low frequency a metallic Hagen-Rubens extrapolation, $R(\omega) = 1 - A\sqrt{\omega}$ was employed, where A is chosen to match the value of the reflectance at the lowest measured frequency. Where an insulating or semiconducting response is observed, below the lowest measured frequency the reflectance was assumed to be constant. Above the highest-measured frequency point the reflectance was assumed to follow a ω^{-1} dependence up to $8 \times 10^4 \text{ cm}^{-1}$, above which a free-electron approximation ($R \propto \omega^{-4}$) was assumed [20]. The complex conductivity, $\tilde{\sigma}(\omega)$, is calculated from the complex dielectric function, $\tilde{\sigma}(\omega) = \sigma_1 + i\sigma_2 = -2\pi i\omega[\tilde{\epsilon}(\omega) - \epsilon_\infty]/Z_0$, where ϵ_∞ high-frequency contribution to the real part of the dielectric function, and $Z_0 \simeq 377 \Omega$ is the impedance of free space.

The temperature dependence of the real part of the optical conductivity for EuCd_2P_2 in the low-frequency region is shown in Fig. 2 for light polarized in the a - b planes. At room temperature, the optical conductivity is that of a poor metal, with $\sigma_1(\omega \rightarrow 0) \simeq 20 \Omega^{-1} \text{ cm}^{-1}$, which is about a factor of

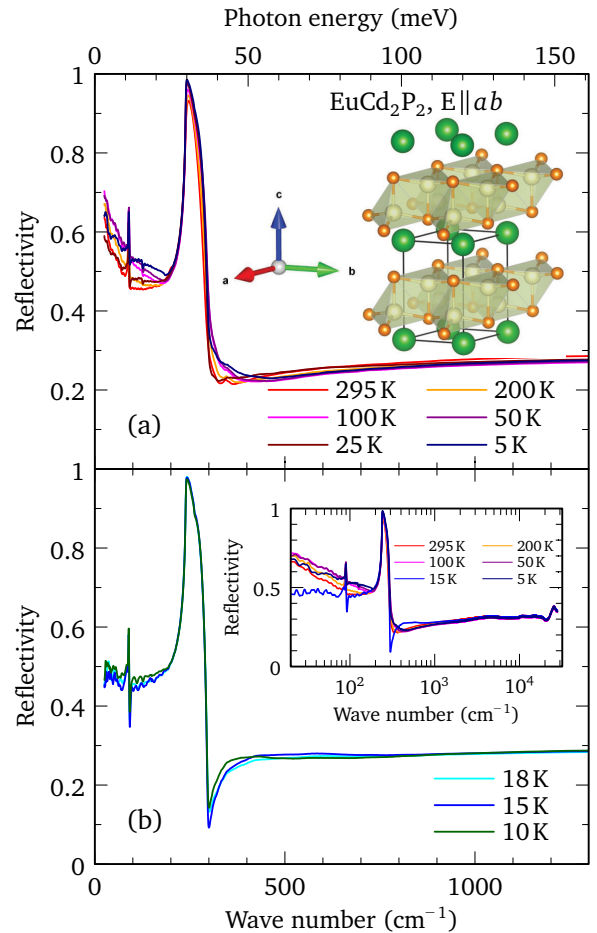


FIG. 1. (a) The temperature dependence of the reflectivity of a single crystal of EuCd_2P_2 versus wave number in the far-infrared region for light polarized in the a - b planes for temperatures between 25 and 295 K, as well as at 5 K, where the response of the reflectivity is metallic. The resolution at low frequency is typically better than 2 cm^{-1} . Inset: the unit cell of EuCd_2P_2 showing the cadmium-phosphide layers, separated by the Eu layers [15]. (b) The reflectivity between 10 and 18 K for light polarized parallel to the a - b planes, where the response is now indicative of an insulating or semiconducting behavior. Inset: the reflectivity on a semilog plot at several temperatures shown over a much wider frequency range.

two lower than the value obtained from transport [13]. Two sharp features, one weak and the other strong, are observed at about 89 and 239 cm^{-1} , respectively. As the temperature is reduced, the low-energy conductivity increases slightly, with $\sigma_1(\omega \rightarrow 0) \simeq 30 \Omega^{-1} \text{ cm}^{-1}$ at 50 K , which is consistent with the decreasing resistivity observed in transport [13], shown in the inset in Fig. 2. At 10 , 15 , and 18 K (for clarity only the conductivity at 15 K is shown in Fig. 2), there is a dramatic decrease in the low-frequency conductivity, with a commensurate transfer of spectral weight (area under the conductivity curve) to high frequency, leading to an increase in the optical conductivity above $\simeq 600 \text{ cm}^{-1}$. Interestingly, below T_N at 5 K the metallic behavior is recovered and spectral weight is transferred back into the free-carrier component.

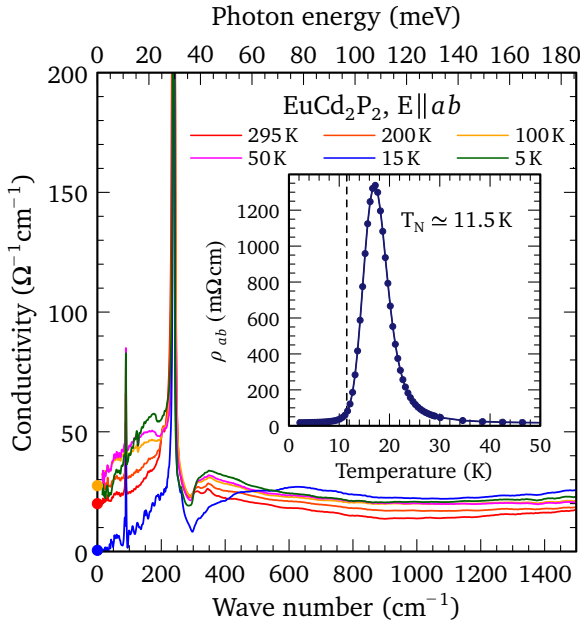


FIG. 2. The temperature dependence of the real part of the optical conductivity of EuCd_2P_2 versus wave number for light polarized in the a - b planes in the low-frequency region. This material is a poor metal; however, at 15 K the response is semiconducting. Two sharp lattice modes are observed at ≈ 89 and 239 cm^{-1} , along with a notchlike feature at about 300 cm^{-1} . The filled circles on the conductivity axis represent the extrapolated values for $\sigma_1(\omega \rightarrow 0)$. Inset: the temperature dependence of the a - b plane dc resistivity measured in zero magnetic field. Note that the resistivity maximum occurs at $\approx 18 \text{ K}$, nearly twice the value of $T_N \approx 11 \text{ K}$ [13].

III. DISCUSSION

To investigate the behavior of the free-carriers in more detail, the optical response is described by the Drude-Lorentz model for the complex dielectric function

$$\tilde{\epsilon}(\omega) = \epsilon_\infty - \frac{\omega_{p,D}^2}{\omega^2 + i\omega/\tau_D} + \sum_j \frac{\Omega_j^2}{\omega_j^2 - \omega^2 - i\omega\gamma_j}. \quad (1)$$

In the first term $\omega_{p,D}^2 = 4\pi n e^2 / m^*$ and $1/\tau_D$ are the square of the plasma frequency and scattering rate for the delocalized (Drude) carriers, respectively, and n and m^* are the carrier concentration and effective mass. In the summation, ω_j , γ_j and Ω_j are the position, width, and strength of a symmetric Lorentzian oscillator that describe the j th vibration or bound excitation.

The strategy that we will adopt in fitting the optical conductivity is to first fit the interband transitions to Lorentzian oscillators using a nonlinear least-squares technique, then, either holding these high-frequency oscillators fixed or allowing only modest refinement, fit the free-carrier response in the low-frequency region. The general approach is to use the minimum number of oscillators required to describe the data. The real part of the in-plane optical conductivity is shown over a wide frequency range at several temperatures in Fig. 3, showing the onset of absorption above $\approx 2000 \text{ cm}^{-1}$, along with the results of the fit at 295 K. Oscillators have been introduced at $\approx 0.54, 0.71, 0.95, 1.45, 2.17, 3.02,$ and 3.50 eV ;

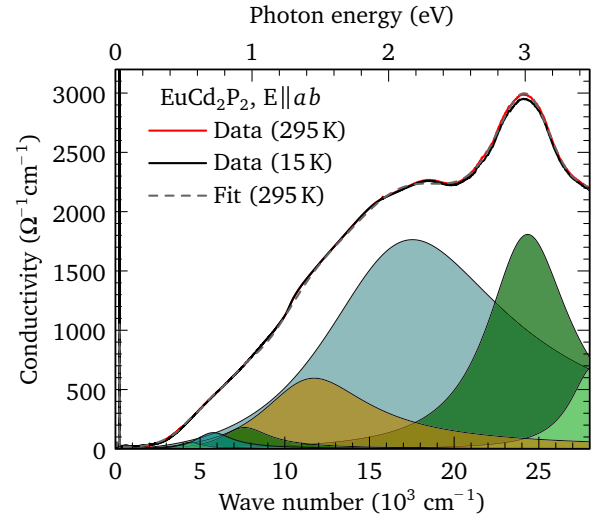


FIG. 3. The optical conductivity of EuCd_2P_2 at 295 and 15 K for light polarized in the a - b planes over a wide frequency range, showing the onset of absorption due to interband transitions at $\approx 2000 \text{ cm}^{-1}$, and the lack of any strong temperature dependence in this region. The result of the fit to the optical conductivity of EuCd_2P_2 at 295 K using the Drude-Lorentz mode is indicated by the dashed line; the fit is decomposed into the contributions from the different Lorentz oscillators.

the fit has been decomposed into the contributions from the Lorentz oscillators. While the overall fit is excellent, it can be argued that the low-frequency oscillator could probably be removed and a reasonable fit still obtained; however, the low-frequency oscillator is required to reproduce the linear region of the optical conductivity, which then allows the low-frequency conductivity to be fit reliably. We also note that because the oscillator at 3.5 eV is at the limit of the measured data, it should be treated with caution.

The determination of the frequencies for the interband transitions allows the low-frequency conductivity to be fit using the Drude model. However, the sharp features attributed to the lattice modes complicate this approach; it is simpler to fit these features and then subtract them from the conductivity, leaving only the electronic continuum associated with the free carriers. Accordingly, the rest of the discussion will first deal with the vibrational properties, followed by an analysis of the free-carrier response.

A. Vibrational properties

In the hexagonal (trigonal) $P\bar{3}m1$ setting, the irreducible vibrational representation for EuCd_2P_2 is $\Gamma_{\text{irr}} = 2A_{1g} + 2E_g + 2A_{2u} + 2E_u$. The A_{1g} and E_g modes are Raman active, while the A_{2u} and E_u modes are infrared active along the c axis and the a - b planes, respectively. The two modes observed in Fig. 2 at ≈ 89 and 239 cm^{-1} are the expected E_u modes. It is tempting to assume that the notchlike feature just above the high-frequency mode at $\approx 300 \text{ cm}^{-1}$ is due to electron-phonon coupling resulting in a Fano-like antiresonance in the electronic continuum [21,22]. However, it should be noted that this vibration is exceptionally strong and narrow; it does not show the broadening that would be expected for a

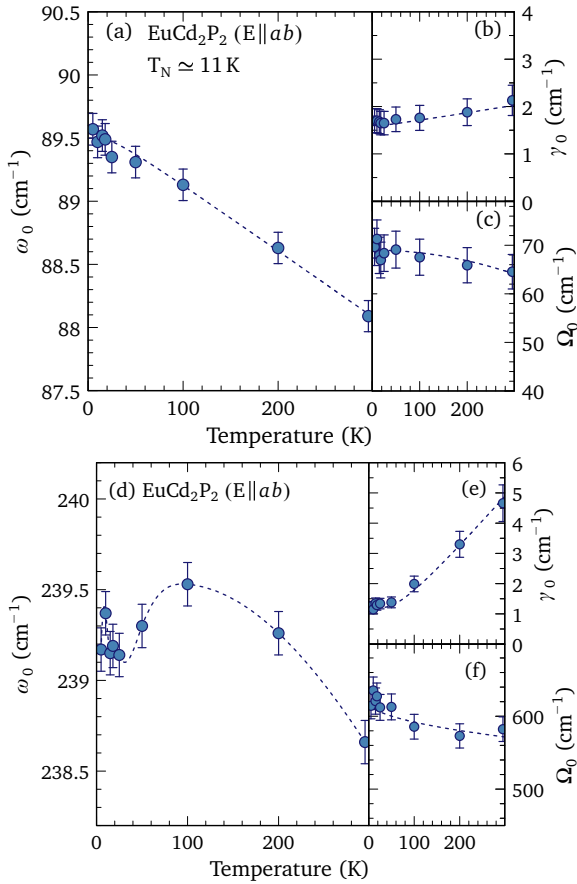


FIG. 4. The results of the fit to the in-plane optical conductivity using symmetric Lorentzian oscillators for the E_u modes in EuCd_2P_2 . The upper panel shows the temperature dependence of (a) the position, (b) line width, and (c) strength of the low-frequency E_u mode; the dashed lines for the position and line width are calculated using the anharmonic decay model using $\omega_B = 89.5 \text{ cm}^{-1}$ ($C = 0.0019$), and $\gamma_0 = 1.6 \text{ cm}^{-1}$ ($\Gamma = 0.032$), respectively. The lower panel shows (d) the position, (e) line width, and (f) strength of the high-frequency E_u mode. The dashed line for the line width is generated using the anharmonic decay model with $\gamma_0 = 1.2 \text{ cm}^{-1}$ ($\Gamma = 1.32$); all others are drawn as a guide to the eye.

mode that was coupled to the electronic background [23]. Moreover, there is almost no electronic background for it to interact with. The low-frequency mode also displays no sign of any asymmetry. The two modes have therefore been fit using a symmetric Lorentzian on a linear background. The results of the fits to the two E_u mode are shown in Fig. 4.

The temperature dependence of the position of the low-energy E_u mode, shown in Fig. 4(a), behaves in the expected way, increasing in frequency (hardening) with decreasing temperature from $\simeq 88$ to about 89.5 cm^{-1} at low temperature. At room temperature this mode is quite narrow with a line width of $\simeq 2 \text{ cm}^{-1}$, and it decreases only slightly to 1.7 cm^{-1} at low temperature; the oscillator strength is roughly constant with $\Omega_0 \simeq 68 \text{ cm}^{-1}$. Overall, this behavior is what is expected for a symmetric anharmonic decay of an optic mode into

two acoustic modes with identical frequencies and opposite momenta [24,25]. The functional form employed here is

$$\omega_0(T) = \omega_B \left[1 - \frac{2C}{e^x - 1} \right], \quad (2)$$

$$\gamma_0(T) = \Gamma_0 \left[1 + \frac{2\Gamma}{e^x - 1} \right], \quad (3)$$

where ω_B is the bare phonon frequency, Γ_0 is a residual line width, C and Γ are constants, and $x = \hbar\omega_B/(2k_B T)$; the bare phonon frequency (residual line width) is recovered in the $T \rightarrow 0$ limit [26]. The model fits are indicated by the dashed lines in Figs. 4(a) and 4(b).

In contrast, the frequency dependence of the high-frequency E_u mode, shown in Fig. 4(d), is somewhat anomalous, initially hardening with decreasing temperature, reaching a maximum of $\simeq 239.5 \text{ cm}^{-1}$ at 100 K before softening by nearly 1 cm^{-1} as the temperature continues to decrease, then hardening again below about 25 K, suggesting a weak coupling to the magnetism in this material. Surprisingly, this mode narrows from $\simeq 5$ to 1.3 cm^{-1} at low temperature in a uniform way, as shown in Fig. 4(e), and can be described by the anharmonic decay model, showing none of the anomalous behavior observed in the position, although there is some evidence the oscillator strength of this mode may increase slightly at low temperature, shown in Fig. 4(f).

The optical conductivity fits were performed with a typical wave number resolution of 1.8 cm^{-1} . Measurements with a resolution of 0.2 cm^{-1} were performed in the far-infrared region above and below T_N and revealed that while the two modes have the same positions as previously reported, the linewidth of the low-frequency mode of $\simeq 0.2 \text{ cm}^{-1}$ suggests it is limited by the resolution of the instrument, while the high-frequency mode has a width of 0.53 cm^{-1} , indicating that this is likely its intrinsic value [18]. Interestingly, neither mode splits below T_N , suggesting the antiferromagnetic ground state does not result in a significant lattice distortion.

B. Electronic response

The determination of the vibrational parameters for the two E_u modes allows these features to be subtracted from the optical conductivity in Fig. 2, resulting in the residual conductivity shown in Fig. 5. There are several things about the residual conductivity that are unusual. The first is that the conductivity is non-Drude; it is initially increasing as a function of frequency, reaching a maximum at $\simeq 200 \text{ cm}^{-1}$ before encountering a notch-like feature between $250 - 300 \text{ cm}^{-1}$. The Drude form for the real part of the optical conductivity may be written as

$$\sigma_1(\omega) = \left(\frac{2\pi}{Z_0} \right) \frac{\omega_{p,D}^2 \tau_D}{1 + \omega^2 \tau_D^2}, \quad (4)$$

which has the form of a Lorentzian centered at zero frequency with a width of $1/\tau_D$.

The origin of the notchlike feature may arise from the terraced nature of the crystal surface, which can introduce structure from the c axis into the ab -plane optical properties. Alternatively, it has been established that in anisotropic media such as the cuprate materials, measuring the

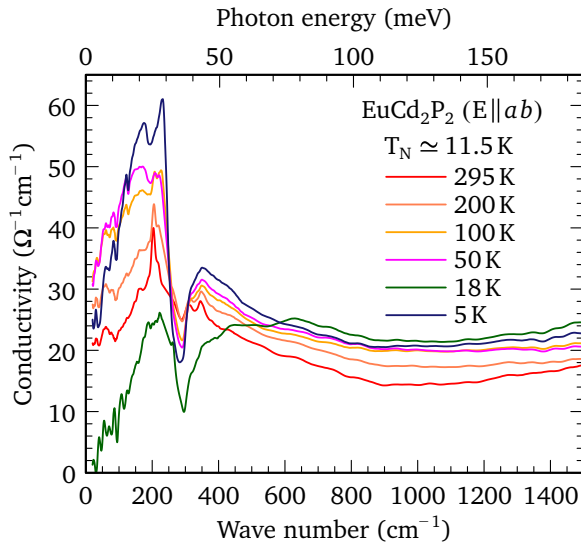


FIG. 5. The temperature dependence of the optical conductivity of EuCd_2P_2 for light polarized in the a - b planes in the far-infrared region with the infrared-active E_u modes removed, revealing the non-Drude response.

reflectivity at anything other than a normal angle of incidence, or having a slightly misoriented surface, can allow c -axis longitudinal optic (LO) modes to manifest themselves as antiresonances (resonances) in the metallic (insulating) electronic background [27–29]. The results from an a - c [(101)] face allows the positions of the A_{2u} transverse optic (TO) modes to be determined and the lower bound of the LO modes to be estimated; comparison with the in-plane results reveal that the artifacts in the a - b plane reflectivity arise from the c -axis TO modes. The terraces lead to a mixing of the in-plane and c -axis reflectivity, thus the notchlike feature is considered to be an artifact and not intrinsic and will be ignored in fits to the residual conductivity; this is discussed in detail in the Supplemental Material [18].

The residual optical conductivity has been fit using the Drude-Lorentz model and the results for two representative fits at 50 and 18 K are shown in Figs. 6(a) and 6(b), respectively; the bound excitations associated with the interband transitions have been held fixed, partly to allow for a more reliable convergence, and also because little temperature dependence of these features is expected (Fig. 3). The quality of the fits are quite good. In the metallic state at 50 K, the Drude response dominates the free-carrier response with $\omega_{p,D} \simeq 1200 \text{ cm}^{-1}$ with a scattering rate of $1/\tau_D \simeq 700 \text{ cm}^{-1}$, values that are representative of a marginally metallic material. A weak bound excitation at $\simeq 180 \text{ cm}^{-1}$ has been included to reproduce the non-Drude response at low frequency; however, it represents only about 10% of the spectral weight associated with the free carriers. At 18 K, the Drude response vanishes and essentially all of the spectral weight associated with free carriers has been transferred to a bound excitation at $\omega_0 \simeq 500 \text{ cm}^{-1}$, with a width $\gamma_0 \simeq 1200 \text{ cm}^{-1}$ and $\Omega_0 \simeq 1200 \text{ cm}^{-1}$. The results of the fits have been summarized in Table I. While the position of the excitation at $\simeq 180 \text{ cm}^{-1}$ shows little temperature dependence, it does increase somewhat in strength below T_N , suggesting that it

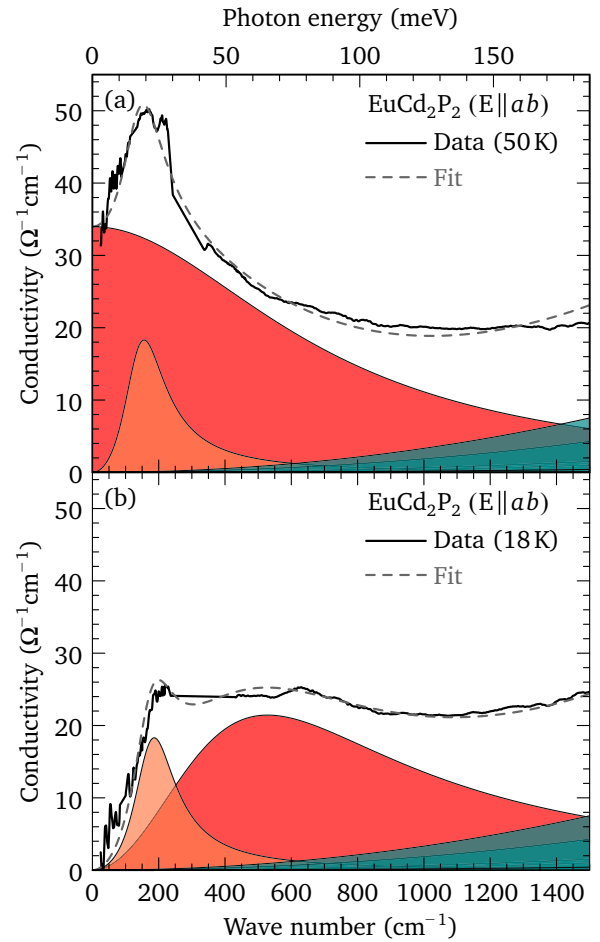


FIG. 6. The fit using the Drude-Lorentz model to the real part of the optical conductivity of EuCd_2P_2 for light polarized in the a - b planes with the infrared-active E_u modes and the notchlike feature removed at (a) 50 K, and (b) 18 K. The fit has been decomposed into the contributions for the free-carrier response as well as the bound excitations. The spectral weight associated with the Drude component is observed to shift to a bound excitation (red curve) with a weaker component that does not change, while the darker colors indicate the low-frequency tails of the mid-infrared absorptions.

is affected by the formation of magnetic order; however, its origin remains unclear.

The temperature dependence of Drude plasma frequency is roughly constant with a value of $\omega_{p,D} \simeq 1150 \pm 150 \text{ cm}^{-1}$. When the Drude term vanishes at temperatures close to the resistivity maximum, the free-carrier spectral weight is transferred into a localized excitation with $\Omega_0 \simeq \omega_{p,D}$, which is also temperature independent. On the other hand, the Drude scattering rate decreases from $1/\tau_D \simeq 760$ to 700 cm^{-1} at 50 K, but then increases dramatically at 25 K, just above the resistivity maximum, to $1/\tau_D \simeq 1270 \text{ cm}^{-1}$. It is tempting to associate the rapid increase in $1/\tau_D$ close to T_N with the scattering of carriers from antiferromagnetic fluctuations. This argument would be reasonable if the maximum in the resistivity occurred just above T_N ; however, it occurs at $\simeq 18 \text{ K}$, nearly twice T_N . Moreover, the resistivity in this material increases by roughly two orders of magnitude, far greater than

TABLE I. The fitted values for the residual optical conductivity of EuCd_2P_2 for light polarized in the a - b planes, consisting of Drude parameters in the metallic state, and a bound excitation in the semiconducting state; the estimated error on the fitted quantities is approximately 10%. All units are in cm^{-1} , unless otherwise indicated.

T (K)	$\omega_{p,D}$	$1/\tau_D$	ω_0	γ_0	Ω_0
295	993	756			
200	1100	753			
100	1160	680			
50	1193	698			
25	1311	1265			
18			486	1180	1183
15			539	1028	1154
10			426	770	1078
5	1170	919			

^aA low-frequency bound excitation is also included at all temperatures to describe the low-frequency conductivity; while its parameters vary, $\omega_0 \approx \gamma_0 \approx 180 \text{ cm}^{-1}$, and $\Omega_0 \approx 400 \text{ cm}^{-1}$, except at 5 K where it increases to $\approx 600 \text{ cm}^{-1}$.

the modest increases that are observed at $\approx T_N$ in the As and Sb compounds.

A more conventional approach relies on polaron effects to describe the transport behavior in the colossal magnetoresistance materials [30–35]. For instance, a transition from large (delocalized carriers) to small polarons (localized carriers) has been used to explain the metal-insulator transition in manganites [36,37]. The application of polarons to this material is attractive because the shape of the electronic absorption is that of an asymmetric Gaussian with a long high-frequency tail [37], which it could be argued, better describes the electronic background in Fig. 6(b) than the two Lorentzian oscillators; additionally, the peak of the localized carriers occurs at $\approx 480 \pm 50 \text{ cm}^{-1}$, which is roughly twice the energy of the high-frequency E_u mode, consistent with a polaronic mechanism. There is several problems with this interpretation. The first is that small lattice polarons are expected to form in systems with strong electron-phonon coupling [35]; however, as previously noted, the narrow line shapes of the infrared-active E_u modes do not support the notion of strong electron-phonon coupling. Additionally, the size of this effect is orders of magnitude smaller than what is observed in the manganites, and finally, no removal of degeneracy due to the coupling of the infrared-active modes to a lattice distortion is observed. Consequently, the polaronic view is not favored.

The most compelling explanation for the dramatic increase of the resistivity above T_N lies in the recent observation of the formation of ferromagnetism at $\approx 2T_N$ [14]; ferromag-

netic clusters form in a paramagnetic background, resulting in carriers becoming localized into spin-polarized clusters due to spin-carrier coupling. Optically, this is observed as the transfer of spectral weight from the free carriers into a localization peak. The resistivity continues to increase until the ferromagnetic regions begin to merge into a contiguous network just above T_N , at which point the resistivity begins to decrease and the spectral weight is transferred back into the free-carrier component. The ferromagnetic regions are observed to persist below T_N in the metallic antiferromagnetic phase where the conductivity has improved slightly, likely due to a decrease in spin fluctuations [38].

IV. CONCLUSIONS

The optical properties of a single crystal of EuCd_2P_2 have been determined for light polarized in the a - b planes above and below T_N over a wide frequency range. At room temperature, the real part of the optical conductivity reveals a marginally metallic material, consisting of a weak free-carrier component with the onset of interband transitions above $\approx 2000 \text{ cm}^{-1}$. Two sharp infrared-active E_u modes are observed at ≈ 89 and 239 cm^{-1} . In addition, a spurious notchlike feature observed in the in-plane conductivity is attributed to c -axis contamination due to terraces in the crystal surface [18]. As the temperature is lowered, there is a modest increase in the low-frequency conductivity; however, below about 50 K the conductivity begins to decrease until at ≈ 18 K (just below $2T_N$), a dramatic change is observed as the majority of the free carriers enter into a localized state, before reverting back to metallic behavior again below T_N . The loss and subsequent restoration of the free-carrier electronic background has a relatively minor effect on the nature of the E_u modes; however, it results in a dramatic change in the line shapes of these vibrations in the reflectivity [18]. The localization of the free carriers is intimately connected with the magnetism in this material. While several scenarios are considered, the prevailing explanation for the resistivity maximum and carrier localization is the formation of ferromagnetic domains below $\approx 2T_N$ that result in spin-polarized clusters due to spin-carrier coupling; once these domains form a contiguous network, the resistivity decreases and the free-carrier component is restored [14].

ACKNOWLEDGMENTS

We would like to acknowledge useful discussions with A. Akrap, V. Sunko, and J. Orenstein. The work at Boston College was funded by the National Science Foundation under Award No. NSF/DMR-2203512. Work at Brookhaven National Laboratory was supported by the Office of Science, U.S. Department of Energy under Contract No. DE-SC0012704.

[1] H. P. Wang, D. S. Wu, Y. G. Shi, and N. L. Wang, Anisotropic transport and optical spectroscopy study on antiferromagnetic triangular lattice EuCd_2As_2 : An interplay between magnetism and charge transport properties, *Phys. Rev. B* **94**, 045112 (2016).

[2] J.-Z. Ma, S. M. Nie, C. J. Yi, J. Jandke, T. Shang, M. Y. Yao, M. Naamneh, L. Q. Yan, Y. Sun, A. Chikina, V. N. Strocov, M. Medarde, M. Song, Y.-M. Xiong, G. Xu, W. Wulfhekkel, J. Mesot, M. Reticcioli, C. Franchini, C. Mudry *et al.*, Spin fluctuation induced Weyl semimetal state in the

- paramagnetic phase of EuCd_2As_2 , *Sci. Adv.* **5**, eaaw4718 (2019).
- [3] L.-L. Wang, N. H. Jo, B. Kuthanazhi, Y. Wu, R. J. McQueeney, A. Kaminski, and P. C. Canfield, Single pair of Weyl fermions in the half-metallic semimetal EuCd_2As_2 , *Phys. Rev. B* **99**, 245147 (2019).
- [4] J. Behrends, R. Ilan, and J. H. Bardarson, Anomalous conductance scaling in strained Weyl semimetals, *Phys. Rev. Res.* **1**, 032028(R) (2019).
- [5] J.-R. Soh, F. de Juan, M. G. Vergniory, N. B. M. Schröter, M. C. Rahn, D. Y. Yan, J. Jiang, M. Bristow, P. Reiss, J. N. Blandy, Y. F. Guo, Y. G. Shi, T. K. Kim, A. McCollam, S. H. Simon, Y. Chen, A. I. Coldea, and A. T. Boothroyd, Ideal Weyl semimetal induced by magnetic exchange, *Phys. Rev. B* **100**, 201102(R) (2019).
- [6] N. H. Jo, B. Kuthanazhi, Y. Wu, E. Timmons, T.-H. Kim, L. Zhou, L.-L. Wang, B. G. Ueland, A. Palasyuk, D. H. Ryan, R. J. McQueeney, K. Lee, B. Schruck, A. A. Burkov, R. Prozorov, S. L. Bud'ko, A. Kaminski, and P. C. Canfield, Manipulating magnetism in the topological semimetal EuCd_2As_2 , *Phys. Rev. B* **101**, 140402(R) (2020).
- [7] H. Su, B. Gong, W. Shi, H. Yang, H. Wang, W. Xia, Z. Yu, P.-J. Guo, J. Wang, L. Ding, L. Xu, X. Li, X. Wang, Z. Zou, N. Yu, Z. Zhu, Y. Chen, Z. Liu, K. Liu, G. Li *et al.*, Magnetic exchange induced Weyl state in a semimetal EuCd_2Sb_2 , *APL Mater.* **8**, 011109 (2020).
- [8] J. Ma, H. Wang, S. Nie, C. Yi, Y. Xu, H. Li, J. Jandke, W. Wulfhekkel, Y. Huang, D. West, P. Richard, A. Chikina, V. N. Strocov, J. Mesot, H. Weng, S. Zhang, Y. Shi, T. Qian, M. Shi, and H. Ding, Emergence of nontrivial low-energy Dirac fermions in antiferromagnetic EuCd_2As_2 , *Adv. Mater.* **32**, 1907565 (2020).
- [9] Y. Xu, L. Das, J. Z. Ma, C. J. Yi, S. M. Nie, Y. G. Shi, A. Tiwari, S. S. Tsirkin, T. Neupert, M. Medarde, M. Shi, J. Chang, and T. Shang, Unconventional Transverse Transport Above and Below the Magnetic Transition Temperature in Weyl Semimetal EuCd_2As_2 , *Phys. Rev. Lett.* **126**, 076602 (2021).
- [10] I. Schellenberg, U. Pfannenschmidt, M. Eul, C. Schwickert, and R. Pöttgen, ^{121}Sb and ^{151}Eu Mössbauer Spectroscopic Investigation of EuCd_2X_2 ($X = \text{P}, \text{As}, \text{Sb}$) and YbCd_2Sb_2 , *Z. Anorg. Allg. Chem.* **637**, 1863 (2011).
- [11] M. C. Rahn, J.-R. Soh, S. Francoual, L. S. I. Veiga, J. Stempffer, J. Mardegan, D. Y. Yan, Y. F. Guo, Y. G. Shi, and A. T. Boothroyd, Coupling of magnetic order and charge transport in the candidate Dirac semimetal EuCd_2As_2 , *Phys. Rev. B* **97**, 214422 (2018).
- [12] J.-R. Soh, E. Schierle, D. Y. Yan, H. Su, D. Prabhakaran, E. Weschke, Y. F. Guo, Y. G. Shi, and A. T. Boothroyd, Resonant x-ray scattering study of diffuse magnetic scattering from the topological semimetals EuCd_2As_2 and EuCd_2Sb_2 , *Phys. Rev. B* **102**, 014408 (2020).
- [13] Z.-C. Wang, J. D. Rogers, X. Yao, R. Nichols, K. Atay, B. Xu, J. Franklin, I. Sochnikov, P. J. Ryan, D. Haskel, and F. Tafti, Colossal magnetoresistance without mixed valence in a layered phosphide crystal, *Adv. Mater.* **33**, 2005755 (2021).
- [14] V. Sunko, Y. S. M. Vranas, C. C. Homes, C. Lee, E. Donoway, Z.-C. Wang, S. Balguri, M. B. Mahendru, A. Ruiz, B. Gunn, R. Basak, E. Schierle, E. Weschke, F. Tafti, A. Frano, and J. Orenstein, Spin-carrier coupling induced ferromagnetism and giant resistivity peak in EuCd_2P_2 , [arXiv:2208.05499](https://arxiv.org/abs/2208.05499).
- [15] K. Momma and F. Izumi, *VESTA 3* for three-dimensional visualization of crystal, volumetric, and morphology data, *J. Appl. Crystallogr.* **44**, 1272 (2011).
- [16] C. C. Homes, M. Reedyk, D. A. Crandles, and T. Timusk, Technique for measuring the reflectance of irregular, submillimeter-sized samples, *Appl. Opt.* **32**, 2976 (1993).
- [17] C. C. Homes, A. W. McConnell, B. P. Clayman, D. A. Bonn, R. Liang, W. N. Hardy, M. Inoue, H. Negishi, P. Fournier, and R. L. Greene, Phonon Screening in High-Temperature Superconductors, *Phys. Rev. Lett.* **84**, 5391 (2000).
- [18] See Supplemental Material at <http://link.aps.org/supplemental/10.1103/PhysRevB.107.045106> for a discussion of how a weak electronic background can fundamentally alter the vibrational line shape in the reflectivity. Examples of terracing in EuCd_2P_2 are shown; the experimental high-resolution (0.2 cm^{-1}) in-plane $[(001)]$ reflectivity, as well as the reflectivity from an a - c $[(101)]$ face is shown. The fitted values of the in-plane E_u and c -axis A_{2u} modes, as well as estimates for the positions of the LO modes, are presented; estimates of ϵ_∞ are validated by examining the positions of the a - b plane TO and LO modes. The analysis concludes that terracing leads to artifacts in the reflectivity due to the simple mixing of the a - b plane and c axis reflectivity.
- [19] M. Dressel and G. Grüner, *Electrodynamics of Solids* (Cambridge University Press, Cambridge, 2001).
- [20] F. Wooten, *Optical Properties of Solids* (Academic Press, New York, 1972), pp. 244–250.
- [21] U. Fano, Effects of configuration interaction on intensities and phase shifts, *Phys. Rev.* **124**, 1866 (1961).
- [22] A. Damascelli, Optical Spectroscopy of Quantum Spin Systems, Ph.D. thesis, University of Groningen, 1996, p. 21.
- [23] Y. Wang, L. Rademaker, E. Dagotto, and S. Johnston, Phonon linewidth due to electron-phonon interactions with strong forward scattering in FeSe thin films on oxide substrates, *Phys. Rev. B* **96**, 054515 (2017).
- [24] P. G. Klemens, Anharmonic decay of optical phonons, *Phys. Rev.* **148**, 845 (1966).
- [25] J. Menéndez and M. Cardona, Temperature dependence of the first-order Raman scattering by phonons in Si, Ge, and α -Sn: Anharmonic effects, *Phys. Rev. B* **29**, 2051 (1984).
- [26] C. C. Homes, Y. M. Dai, J. Schneeloch, R. D. Zhong, and G. D. Gu, Phonon anomalies in some iron telluride materials, *Phys. Rev. B* **93**, 125135 (2016).
- [27] D. W. Berreman, Resonant reflectance anomalies: Effect of shapes of surface irregularities, *Phys. Rev. B* **1**, 381 (1970).
- [28] M. Reedyk and T. Timusk, Evidence for a - b -Plane Coupling to Longitudinal c -Axis Phonons in High- T_c Superconductors, *Phys. Rev. Lett.* **69**, 2705 (1992).
- [29] C. C. Homes, J. M. Tranquada, and D. J. Buttrey, Stripe order and vibrational properties of $\text{La}_2\text{NiO}_{4+\delta}$ for $\delta = 2/15$: Measurements and *ab initio* calculations, *Phys. Rev. B* **75**, 045128 (2007).
- [30] D. Emin, Optical properties of large and small polarons and bipolarons, *Phys. Rev. B* **48**, 13691 (1993).
- [31] A. S. Alexandrov and N. Mott, *Polarons & Bipolarons* (World Scientific, Cambridge, 1995).
- [32] A. J. Millis, R. Mueller, and B. I. Shraiman, Fermi-liquid-to-polaron crossover. II. Double exchange and the physics of colossal magnetoresistance, *Phys. Rev. B* **54**, 5405 (1996).

- [33] H. Röder, J. Zang, and A. R. Bishop, Lattice Effects in the Colossal-Magnetoresistance Manganites, *Phys. Rev. Lett.* **76**, 1356 (1996).
- [34] J. D. Lee and B. I. Min, Polaron transport and lattice dynamics in colossal-magnetoresistance manganites, *Phys. Rev. B* **55**, 12454 (1997).
- [35] M. B. Salamon and M. Jaime, The physics of manganites: Structure and transport, *Rev. Mod. Phys.* **73**, 583 (2001).
- [36] A. Lanzara, N. L. Saini, M. Brunelli, F. Natali, A. Bianconi, P. G. Radaelli, and S.-W. Cheong, Crossover from Large to Small Polarons across the Metal-Insulator Transition in Manganites, *Phys. Rev. Lett.* **81**, 878 (1998).
- [37] C. Hartinger, F. Mayr, J. Deisenhofer, A. Loidl, and T. Kopp, Large and small polaron excitations in $\text{La}_{2/3}(\text{Sr/Ca})_{1/3}\text{MnO}_3$ films, *Phys. Rev. B* **69**, 100403(R) (2004).
- [38] Y. Zhang, F. Chen, C. He, L. X. Yang, B. P. Xie, Y. L. Xie, X. H. Chen, M. Fang, M. Arita, K. Shimada, H. Namatame, M. Taniguchi, J. P. Hu, and D. L. Feng, Strong correlations and spin-density-wave phase induced by a massive spectral weight redistribution in $\alpha\text{-Fe}_{1.06}\text{Te}$, *Phys. Rev. B* **82**, 165113 (2010).